Applied Energy 339 (2023) 120975

Contents lists available at ScienceDirect

Applied Energy

journal homepage: www.elsevier.com/locate/apenergy

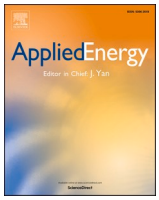

High-pressure supersonic carbon dioxide (CO_2) separation benefiting carbon capture, utilisation and storage (CCUS) technology

Hongbing Ding [a], Yu Zhang [a], Yuanyuan Dong [a], Chuang Wen [b], Yan Yang [b,*]

[a] Tianjin Key Laboratory of Process Measurement and Control, School of Electrical and Information Engineering, Tianjin University, Tianjin 300072, China
[b] Faculty of Environment, Science and Economy, University of Exeter, Exeter EX4 4QF, United Kingdom

HIGHLIGHTS

- A novel decarbonization concept applied to offshore natural gas wells benefiting CCUS technology.
- A comprehensive CFD model considers real gas EOS and the behaviours of gas, droplets, liquid film.
- Compatible with pure CO_2 and CH_4-CO_2 models to study condensation and separation characteristics.
- The maximum CO_2 condensation amount under high pressure and low temperature is 10.33 ton/h.
- The maximum CO_2 capture capacity is 4.43 ton/h with high heterogeneous droplet mass concentration.

ARTICLE INFO

Keywords:
Carbon capture
CO_2 separation
CO_2 capture
Supersonic separation
CCS
CCUS

ABSTRACT

Carbon capture, utilisation and storage (CCUS) is of unique significance for building a green and resilient energy system, and it is also a key solution to tackle the climate challenge. The concept of supersonic decarburization, a joint product of non-equilibrium condensation and swirling separation, can contribute to CCUS technology in a clean way. In this paper, a numerical model is established and validated to investigate the complex physical phenomena of supersonic decarbonization in a high-pressure environment based on the real gas equation of state. The model is compatible with the pure CO_2 model and CH_4-CO_2 model. Through the simulation of the supersonic nozzle and supersonic separator, the condensation and separation performance of supersonic decarbonization technology was evaluated. For the condensation performance of carbon dioxide, the results show that higher pressure makes it much easier to achieve the condensation process. When the pressure is supercritical, the decrease of inlet temperature or the increase of inlet mole fraction of CO_2 leads to a higher liquid fraction. For separation performance, when the mass concentration of inlet heterogeneous droplets increases from 0.1 kg/m^3 to 7.5 kg/m^3, the carbon separation amount increases from 3.33 ton/h to 4.43 ton/h, while the exergy loss of condensed CO_2 drops from 436.57 kJ/kg to 329.56 kJ/kg. It demonstrates that the decarburization process is easier, and exergy required for condensation decreases when the concentration of the foreign core is larger. This new concept is beneficial to CCUS technology and can be applied to carbon capture in offshore natural gas processing.

1. Introduction

The emission of the greenhouse gas carbon dioxide (CO_2) is becoming a potential threat to human existence and creation [1]. Therefore, the sustainable development of energy systems is recognised as one of the top priorities, and it is a globalization proposition to limit the global temperature rise to 1.5 ℃ above the pre-industrial level [2,3]. Carbon capture, utilisation and storage (CCUS), is an important and potentially effective climate mitigation technology, which captures carbon dioxide emissions from fossil power generation and industrial processes for reuse or storage [4–6]. In terms of carbon capture, the advantages and disadvantages of existing decarbonization technologies are listed in Table 1, from which it can be seen that the limitations of traditional decarbonization technologies such as absorption [7–9], adsorption [10–12], membrane [13,14], cyclone [15] and cryogenics [16] are corrosive, complicated machinery, environmental pollution,

* Corresponding author.
E-mail addresses: yanyang2021@outlook.com, y.yang7@exeter.ac.uk (Y. Yang).

https://doi.org/10.1016/j.apenergy.2023.120975
Received 29 October 2022; Received in revised form 15 February 2023; Accepted 10 March 2023
Available online 28 March 2023

low utilization rate, etc., which are gradually decoupled from the global energy call [17,18]. Therefore, the further development of the cost-effective and high-efficient methods benefiting CCUS technology should be focused on.

Supersonic separation is a revolutionary separation method with low cost, no pollution, and high efficiency [19–21]. As shown in Fig. 1 (a), the mixed gas can be cooled and condensed into droplets by a supersonic nozzle, and then the swirl generated by the swirl generator can push the droplets to the wall to form the liquid film. The liquid film will be separated from the liquid outlet, and the outcome is that the proportion of condensable components in the mixture decreases [22]. This separation method can provide a new way for decarbonization, and the key to understanding this new concept is carbon condensation in a supersonic nozzle. Fig. 1 (b) is used to explain this mechanism. Superheated steam or mixed gas expands along the nozzle from the nozzle inlet (State 1), and in the process, the gas pressure decreases, and the supercooling increases. The gas at a certain section behind the throat of the nozzle will reach a saturation state and the supercooling will increase to zero (State 2). If the gas does not contain any foreign core, condensation will not occur here [23]. The gas continues to expand into supersaturated or supercooled steam. When the gas state reaches Wilson point (State 3), a large number of condensation nuclei suddenly appear, and then vapour molecules condense on the condensation nuclei to form droplets and grow up gradually. After the above condensation process, vapour quickly changes from a non-equilibrium supersaturated state to a state close to thermodynamic equilibrium (State 4) [24]. Generally speaking, the characteristics of non-equilibrium condensation in supersonic expansion flow strongly depend on the coupling between the flow field and CO_2 condensation. Accurate prediction of CO_2 condensation flow needs to emphasize physical characteristics such as carbon properties, turbulence, two-phase slip, interphase mass transfer, and latent heat [25].

In recent years, more attention has been paid to the numerical simulation of condensation in supersonic flow. Castier et al. [26] considered single-phase flow and phase equilibrium processes at the same time, numerically simulated natural gas flow in a supersonic nozzle, and rigorously evaluated thermodynamic properties. Chen et al. [27] established a condensation flow model of CH_4-CO_2 two-component gas by using computational fluid dynamics (CFD) software for a supersonic nozzle and systematically studied the influence of different nozzle structures on CO_2 condensation. Niknam et al. [28] carried out a numerical analysis of condensation parameters in supersonic flow. The nozzle geometry was fixed, and the temperature, pressure, and gas type were changed to evaluate the nozzle performance and cooling capacity. Wen et al. [29] carried out numerical research and experimental validation on the decarbonization of natural gas in high-pressure supersonic flow and found that the CO_2 condensation predicted by ideal gas EOS had a great deviation from the real value under high pressure. On this basis, in our recent research [30], a two-fluid model considering real gas EOS was developed, and the thermodynamic and kinetic characteristics of CO_2 at Wilson point in a supersonic nozzle were studied in detail. In addition to carbon condensation, another key link in the proposed concept of supersonic decarbonization is the separation of carbon dioxide from the equipment, which depends on the existence of swirling flow, so that the condensed droplets are thrown to the wall and deposited into the liquid film. Chen et al. [31] established and verified a two-component steam (CO_2-N_2) condensation model, and studied the non-equilibrium CO_2 condensation in flue gas under the coexistence of supersonic flow and swirling flow. The results showed that swirling flow made the nucleation start point move to the nozzle throat. Yue et al. [32] coupled the two-fluid model with the Eulerian wall film model and studied the effect of liquid velocity on liquid film flows in a cylinder cyclone. The results show that the high liquid velocity damages the uniformity of the liquid film. Li et al. [33] used a similar model to study the two-phase boiling flow. The simulation results show that the model can capture the drastic temperature drift well. Chen et al. [34] also proposed a combination of the Eulerian-Eulerian model and the thin film model to simulate the coating deposition process when spraying curved surfaces with a moving spray gun. Ding et al. [35] extended this numerical model to a supersonic separator to simulate the flow of gas, liquid droplets, and liquid film in supersonic swirling flows, taking into account the effects of homogeneous and heterogeneous condensation. However, the separation object studied is water vapour, which has different physical properties from CO_2 [36], especially under high-pressure operating conditions.

From the literature review, there is still a lack of simulation and experimental research on the condensation and separation of supercritical carbon dioxide by supersonic decarbonization technology. The purpose of this study is to evaluate the effectiveness of non-equilibrium condensation and swirl separation of CO_2 in the concept of supersonic decarburization, which will contribute to the development of CCUS and capture CO_2 more purely. To this end, a numerical model integrating a two-fluid model and liquid film model suitable for CO_2 condensation was established and validated, which uses a real gas EOS and considers swirl and liquid film. The model is compatible with the pure CO_2 system and CH_4-CO_2 system, and for the sake of being closer to the actual industry [37–39], the high-pressure condition is our main research scope. In this foundation, using the pure CO_2 model, the difference between real gas EOS and ideal gas EOS in simulated carbon condensation flow was clarified, and the conditions more suitable for CO_2 condensation were obtained. Using the CH_4-CO_2 model, the effects of inlet temperature and inlet CO_2 mole fraction on condensation were explored, and the effects of inlet heterogeneous CO_2 mass concentration on separation were studied. The main contribution of this study is to provide an

Table 1
Advantages and disadvantages of existing decarbonization technologies.

Decarburization technology	Application	Advantage	Disadvantage
Absorption [7–9]	TEG	(a) High dew point depression (b) Low energy consumption	(a) Complex process (b) High cost (c) Corrosive (d) Difficult to regenerate
Adsorption [10–12]	Fixed Bed Adsorption Tower, NHD	(a) Simple process (b) High decarbonization rate	(a) High cost (b) Low energy utilization rate (c) Corrosive
Membrane [13,14]	Polyimide	(a) Simple process (b) No additive (c) No secondary pollution (d) Low energy consumption	(a) Corrosive membrane (b) Harsh pretreatment process
Cyclone [15]	Cyclone separator	(a) Simple process (b) Low cost	(a) Low decarbonization efficiency
Cryogenics [16]	J–T valve, turboexpander	(a) Simple process (b) High operational flexibility (c) High decarbonization efficiency	(a) High energy consumption (b) High dew point (c) Easy to form hydrate

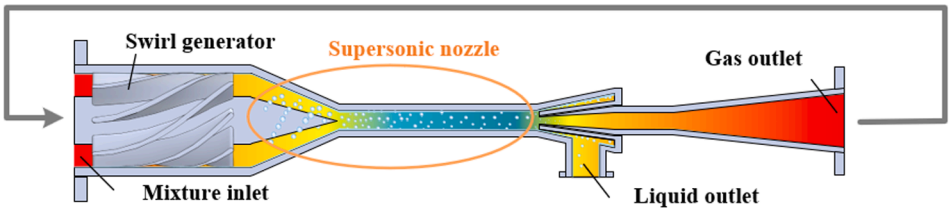

(a) Supersonic decarbonization concept applied to CCUS technology

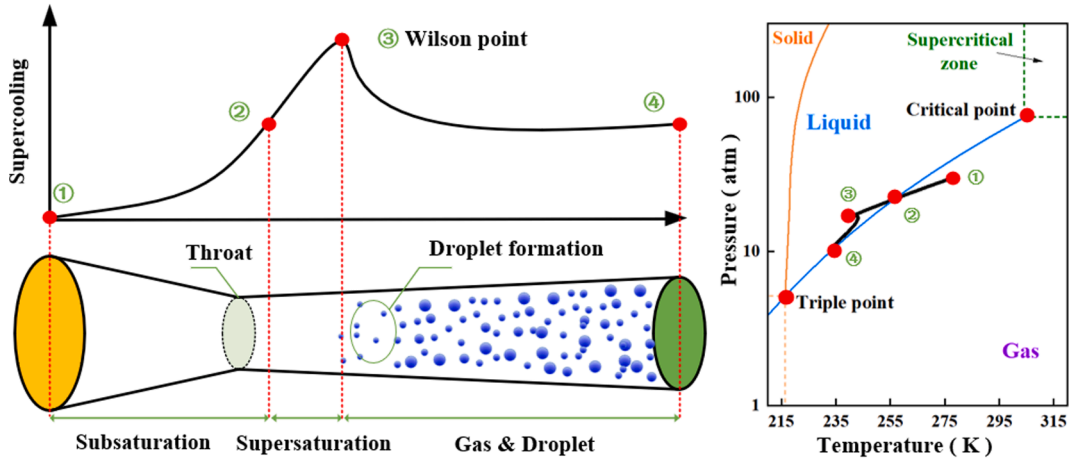

(b) Non-equilibrium condensation in supersonic nozzle

Fig. 1. A novel concept for CO_2 separation in supersonic flows.

innovative technology choice and a comprehensive numerical basis for CCUS technology which is beneficial for climate mitigation.

2. Modelling and validation

The composition, implementation, and validation of the proposed numerical model capable of simulating both pure CO_2 and CH_4-CO_2 systems in supersonic flows are introduced in this section.

2.1. Two-phase flow modelling considering non-equilibrium phase transitions

The established model is an integration of the gas phase equations, homogeneous/heterogeneous condensation model, Eulerian wall film model, and heat-mass transfer among gas, droplets, and liquid film. The model is based on the following assumptions:

(1) Spherical droplets;
(2) Both homogeneous and heterogeneous condensations are considered;
(3) The latent heat released by condensation is added to the source term of the gas phase;
(4) The interphase slips and drag force are considered;
(5) The collision, deposition, and entrainment of droplets are considered.

2.1.1. Modelling of the gas, droplet, and liquid film

The mass, momentum, and energy conservation equations, along with the species transport equations, for pure CO_2 or a mixture of CH_4 and CO_2 are given by

$$\frac{\partial}{\partial t}\left(\alpha_g\rho_g\right)+\nabla\cdot\left(\alpha_g\rho_g\vec{u}_g\right)=-\left(\dot{m}_{\mathrm{hom}}+\dot{m}_{het}\right) \tag{1}$$

$$\frac{\partial}{\partial t}\left(\alpha_g\rho_g\vec{u}_g\right)+\nabla\cdot\left(\alpha_g\rho_g\vec{u}_g\vec{u}_g\right)=-\alpha_g\nabla p+\nabla\cdot\left(\alpha_g\bar{\bar{\tau}}_{eff}\right)+\alpha_g\rho_g\vec{g}-\left(\dot{m}_{\mathrm{hom}}+\dot{m}_{het}\right)\vec{u}_g-\vec{F}_D \tag{2}$$

$$\frac{\partial}{\partial t}\left(\alpha_g\rho_g E\right)+\nabla\cdot\left[\alpha_g\left(\rho_g E+p\right)\vec{u}_g\right]=\nabla\cdot\left[\alpha_g\lambda_{eff}\nabla T_g-\alpha_g\sum_i h_i\vec{J}_i+\alpha_g\left(\bar{\bar{\tau}}_{eff}\cdot\vec{u}_g\right)\right]-\left(\dot{m}_{\mathrm{hom}}+\dot{m}_{het}\right)h_{\mathrm{lg}} \tag{3}$$

$$\frac{\partial}{\partial t}\left(\alpha_g\rho_g Y_i\right)+\nabla\cdot\left(\alpha_g\rho_g\vec{u}_g Y_i\right)=-\nabla\cdot\left(\alpha_g\vec{J}_i\right)+S_i \tag{4}$$

where α, ρ, $\vec{u}$, p, E, and T represent physical quantities of volume fraction, density, velocity, energy, and temperature, respectively. The subscripts g and i represent the gas phase and species, respectively. $\dot{m}$ represents the mass transfer rate (kg m^{-3} s^{-1}), and its subscripts hom, and het denote mass transfer from homogeneous droplets, and heterogeneous droplets, respectively. h_{lg} is the latent heat, $\vec{g}$ is the gravity vector, $\vec{F}_{\mathrm{D}}$ is the drag force between the gas phase and the droplet (N m^3), $\bar{\bar{\tau}}_{\mathrm{eff}}$ is the effective thermal conductivity, and $\vec{J}$ is the diffusion flux of species i. Y_{i} represents the mass fraction of species i. S_{i} is the mass change between species where the value is $-\left(\dot{m}_{\mathrm{hom}}+\dot{m}_{\mathrm{het}}\right)$ for the species of CO_2.

The governing equations of the CO_2 droplet phase include the droplet mass conservation equation, droplet momentum conservation equation, and droplet number concentration transport equation.

$$\begin{cases} \frac{\partial}{\partial t}(\alpha_{\mathrm{hom}}\rho_l) + \nabla\cdot\left(\alpha_{\mathrm{hom}}\rho_l \vec{u}_{\mathrm{hom}}\right) = \dot{m}_{\mathrm{hom}} - \dot{m}_{\mathrm{col}} \\ \frac{\partial}{\partial t}(\alpha_{\mathrm{het}}\rho_l) + \nabla\cdot\left(\alpha_{\mathrm{het}}\rho_l \vec{u}_{\mathrm{het}}\right) = \dot{m}_{\mathrm{het}} + \dot{m}_{\mathrm{col}} \end{cases} \tag{5}$$

$$I = \frac{\upsilon\rho_{\mathrm{g}}^2}{S_{\mathrm{s}}}\sqrt{\frac{2\sigma}{\pi m_m^5}}\exp\left(-\frac{16\pi}{3}\frac{\upsilon^2\sigma^3}{\left(k_{\mathrm{B}}T_{\mathrm{g}}\right)^3\left(\ln S_{\mathrm{s}}\right)^2}\right) \tag{12}$$

$$r_{\mathrm{c}} = \frac{2\sigma}{\rho_l R_{\mathrm{v}} T_{\mathrm{g}} \ln(S_{\mathrm{s}})} \tag{13}$$

$$\begin{cases} \frac{\partial}{\partial t}\left(\alpha_{\mathrm{hom}}\rho_l \vec{u}_{\mathrm{hom}}\right) + \nabla\cdot\left(\alpha_{\mathrm{hom}}\rho_l \vec{u}_{\mathrm{hom}}\vec{u}_{\mathrm{hom}}\right) = -\alpha_{\mathrm{hom}}\nabla p + \alpha_{\mathrm{hom}}\rho_l \vec{g} + \left(\dot{m}_{\mathrm{hom}} - \dot{m}_{\mathrm{col}}\right)\vec{u}_{\mathrm{hom}} + \vec{F}_{\mathrm{D,hom}} \\ \frac{\partial}{\partial t}\left(\alpha_{\mathrm{het}}\rho_l \vec{u}_{\mathrm{het}}\right) + \nabla\cdot\left(\alpha_{\mathrm{het}}\rho_l \vec{u}_{\mathrm{het}}\vec{u}_{\mathrm{het}}\right) = -\alpha_{\mathrm{het}}\nabla p + \alpha_{\mathrm{het}}\rho_l \vec{g} + \left(\dot{m}_{\mathrm{het}} + \dot{m}_{\mathrm{col}}\right)\vec{u}_{\mathrm{het}} + \vec{F}_{\mathrm{D,het}} \end{cases} \tag{6}$$

$$\begin{cases} \frac{\partial n_{\mathrm{hom}}}{\partial t} + \nabla\cdot\left(n_{\mathrm{hom}}\vec{u}_{\mathrm{hom}}\right) = I - N_{\mathrm{col}} \\ \frac{\partial n_{\mathrm{het}}}{\partial t} + \nabla\cdot\left(n_{\mathrm{het}}\vec{u}_{\mathrm{het}}\right) = 0 \end{cases} \tag{7}$$

where ρ_l is the droplet density. $\dot{m}_{\mathrm{col}}$(kg m^{-3} s^{-1}) is the mass source term due to collision and coalescence between homogeneous and heterogeneous droplets, N_{col} (m^{-3} s^{-1}) is also the source term due to collision. $\vec{F}_{\mathrm{D,hom}}$ and $\vec{F}_{\mathrm{D,het}}$ are drag forces between gas and CO_2 droplets, $\vec{F}_{\mathrm{D,hom}} + \vec{F}_{\mathrm{D,het}} = \vec{F}_{\mathrm{D}}$. n_{hom} and n_{het} (m^{-3}) are the droplet number concentration, meaning the number of homogenous and heterogeneous droplets per unit volume.

For the supersonic separator, the presence of the rotating field causes the droplets to hit the wall and transform into liquid films. The conservation equations are given by [40]

$$\frac{\partial}{\partial t}(\rho_l\delta) + \nabla_s\cdot\left(\rho_l\delta\vec{u}_f\right) = \delta\left(\dot{m}_d - \dot{m}_{film}\right) \tag{8}$$

$$\frac{\partial}{\partial t}\left(\rho_l\delta\vec{u}_f\right) + \nabla_s\cdot\left(\rho_l\delta\vec{u}_f\vec{u}_f\right) = -\delta\nabla_s p + \rho_l\delta\vec{g}_\tau + \frac{3}{2}\vec{\tau}_{fs} - \frac{3\mu_l}{\delta}\vec{u}_f + \delta\left(\dot{m}_d - \dot{m}_{film}\right)\vec{u}_f \tag{9}$$

$$\frac{\partial}{\partial t}\left(\rho_l\delta h_f\right) + \nabla_s\cdot\left(\rho_l\delta h_f\vec{u}_f\right) = \frac{\lambda_l}{\delta}(T_s + T_w - 2T_m) + \delta\left(\dot{m}_d - \dot{m}_{film}\right)h_{\mathrm{lg}} \tag{10}$$

where ∇_s is the surface gradient. δ is the film thickness. The subscript f represents the liquid film. $\vec{g}_\tau$ is the gravity component parallel to the film. T_s, T_w, and T_m are the film surface, wall, and film half-depth temperature, respectively.$\dot{m}_d$ is mass transfer rate due to the deposition of homogeneous and heterogeneous droplets,$\dot{m}_d = \dot{m}_{d,hom} + \dot{m}_{d,het}$.$\dot{m}_{film}$ represents film phase change rate between gas and film.

2.1.2. Calculation of source terms

The mass exchange due to evaporation and condensation between the gas phase and droplets is denoted by $\dot{m}_{\mathrm{hom}}$ and $\dot{m}_{\mathrm{het}}$ in Eq. (1):

$$\begin{cases} \dot{m}_{\mathrm{hom}} = I\rho_l\frac{4\pi r_{\mathrm{c}}^3}{3} + n_{\mathrm{hom}}\rho_l 4\pi r_{\mathrm{hom}}^2\frac{dr_{\mathrm{hom}}}{dt}, \\ \dot{m}_{\mathrm{het}} = n_{\mathrm{het}}\rho_l 4\pi r_{\mathrm{het}}^2\frac{dr_{\mathrm{het}}}{dt} \end{cases} \tag{11}$$

where the homogeneous nucleation rate I (m^{-3} s^{-1}) and the critical nucleation radius of the droplet r_{c} are computed by

where υ is the volume of a single liquid molecule, m_{m} is the mass of the single liquid molecule. k_{B} is Boltzmann's constant. S_{s} means supersaturation, equal to $p_{\mathrm{v}}/p_{\mathrm{sat}}(T_{\mathrm{g}})$, where the subscript 'sat' represents the saturation state. σ is the liquid surface tension (N/m). R_{v} represents the specific gas constant. Besides, the mean radii r_{hom} and r_{het} in Eq. (11) are expressed as

$$r_{\mathrm{hom}} = \left(\frac{3\alpha_{\mathrm{hom}}}{4\pi n_{\mathrm{hom}}}\right)^{\frac{1}{3}},\ r_{\mathrm{het}} = \left(\frac{3\alpha_{\mathrm{het}}}{4\pi n_{\mathrm{het}}}\right)^{\frac{1}{3}} \tag{14}$$

The growth rates of both homogeneous and heterogeneous droplets are calculated by

$$\frac{dr}{dt} = \frac{\sum_{i=1}^{2}a_i}{\rho_l h_{\mathrm{lg}}}(T_{\mathrm{r}} - T_{\mathrm{v}}) \tag{15}$$

$$T_{\mathrm{r}} = T_{\mathrm{sat}} - \Delta T\frac{r_{\mathrm{c}}}{r} \tag{16}$$

where the subscript 'v' represents CO_2 vapour. a_{i} is the heat transfer coefficient for species i [41]. T_{r} is the droplet surface temperature. ΔT is supercooling, $\Delta T = T_{\mathrm{sat}}$ - T_{g}.

The drag force in Eq. (2) is defined as [42]

$$\begin{cases} \vec{F}_{\mathrm{D,hom}} = \frac{9\mu_{\mathrm{g}}}{2r_{\mathrm{hom}}^2}C_{\mathrm{D}}\frac{\mathrm{Re}_{\mathrm{p,\,hom}}}{24}\alpha_{\mathrm{hom}}\left(\vec{u}_{\mathrm{hom}} - \vec{u}_{\mathrm{g}}\right) \\ \vec{F}_{\mathrm{D,het}} = \frac{9\mu_{\mathrm{g}}}{2r_{\mathrm{het}}^2}C_{\mathrm{D}}\frac{\mathrm{Re}_{\mathrm{p,\,het}}}{24}\alpha_{\mathrm{het}}\left(\vec{u}_{\mathrm{het}} - \vec{u}_{\mathrm{g}}\right) \end{cases} \tag{17}$$

where the relative Reynolds number $\mathrm{Re}_{\mathrm{p,hom}}$ and $\mathrm{Re}_{\mathrm{p,het}}$ are

$$\begin{cases} \mathrm{Re}_{\mathrm{p,hom}} = 2\rho_{\mathrm{g}}r_{\mathrm{hom}}\left|\vec{u}_{\mathrm{hom}} - \vec{u}_{\mathrm{g}}\right|\Big/\mu_{\mathrm{g}} \\ \mathrm{Re}_{\mathrm{p,het}} = 2\rho_{\mathrm{g}}r_{\mathrm{het}}\left|\vec{u}_{\mathrm{het}} - \vec{u}_{\mathrm{g}}\right|\Big/\mu_{\mathrm{g}} \end{cases}$$

The drag coefficient C_{D} is calculated as [43]

$$C_{\mathrm{D}} = \begin{cases} \frac{24}{\mathrm{Re}_{\mathrm{p}}},\ \mathrm{Re}_{\mathrm{p}} \leqslant 1 \\ \frac{24}{\mathrm{Re}_{\mathrm{p}}}\left(1 + 0.15\mathrm{Re}_{\mathrm{p}}^{0.687}\right),\ 1 < \mathrm{Re}_{\mathrm{p}} \leqslant 1000 \\ 0.3455,\ \mathrm{Re}_{\mathrm{p}} > 1000 \end{cases} \tag{19}$$

The source term of Eq. (5) and Eq. (7) for collision and coalescence are [44]

$$\begin{cases} \dot{m}_{\mathrm{col}} = n_{\mathrm{het}} f \rho_l \dfrac{4\pi r_{\mathrm{hom}}^3}{3} \\ N_{\mathrm{col}} = n_{\mathrm{het}} f \\ f = n_{\mathrm{hom}} \pi (r_{\mathrm{het}} + r_{\mathrm{hom}})^2 \left| \vec{u}_{\mathrm{het}} - \vec{u}_{\mathrm{g}} \right| \end{cases} \tag{20}$$

where f is the mean collision frequency.

$\dot{m}_{\mathrm{d}}$ in Eq. (8) is given by

$$\dot{m}_{\mathrm{d}} = \dot{m}_{\mathrm{d,hom}} + \dot{m}_{\mathrm{d,het}} = \frac{\alpha_{\mathrm{hom}} \rho_l \vec{u}_{\mathrm{hom}} \cdot \vec{n}}{\delta} + \frac{\alpha_{\mathrm{het}} \rho_l \vec{u}_{\mathrm{het}} \cdot \vec{n}}{\delta} \tag{21}$$

where $\vec{n}$ is the normal vector of the film area, that is, perpendicular to the direction of liquid film flow. Here, we consider the mass transfer at the boundary of the liquid film to be the dot product of the term in the left bracket in Eq. (6) with the normal vector of the film area.

The phase change rate between the liquid film and gas phase $\dot{m}_{\mathrm{film}}$ is calculated by [45]

$$\dot{m}_{\mathrm{film}} = \frac{1}{\delta} \frac{\rho_{\mathrm{g}} M / D}{\rho_{\mathrm{g}} M / D + C_{\mathrm{phase}}} C_{\mathrm{phase}} (Y_{\mathrm{sat}} - Y) \tag{22}$$

where D represents cell-centre-to-wall distance, and M is the mass diffusivity of CO_2 vapour. C_{phase} is the phase change constant. Y_{sat} represents the saturation mass fraction of CO_2 vapour.

2.1.3. Thermodynamic property modelling

In physics and thermodynamics, an equation of state (EOS) is an equation that describes the thermodynamic state of a material under given physical conditions, which provides a mathematical relationship between three or more related "state variables" such as temperature, pressure, volume, or internal energy. The ideal gas EOS is not precise enough when the temperature is very low or the pressure is high, so a suitable real gas EOS plays a key role in high-pressure supersonic flow [46].

The NIST Real Gas Model uses the National Institute of Standards and Technology (NIST) Thermodynamic and Transport Properties Database for Refrigerants and Refrigerant Mixtures Version 9.1 (REFPROP v9.1) to evaluate the thermodynamics and transport of approximately 125 fluids or mixtures of these fluids properties, including methane and carbon dioxide [47]. For pure CO_2, the REFPROP v9.1 database uses the precise EOS for pure fluids provided by NIST. These equations are based on three-state equations, modified Benedict-Webb-Rubin (MBWR) EOS, Helmholtz-energy EOS, and extended corresponding states (ECS) [30]. For a mixed fluid composed of CH_4 and CO_2, the thermodynamic properties were calculated using the mixing rule applied to the Helmholtz-energy EOS of the mixture components [48].

2.2. Numerical method

Ansys fluent software is used for numerical calculation, and the user-defined function is written and coupled with the solver of the software itself. User-defined-scalar equations are defined to calculate the conservation of droplets, and user-defined memories are defined to store the values of physical quantities of interest. For the supersonic nozzle, the standard k-epsilon model is used for turbulence. For the supersonic separator, the Reynolds stress model (RSM) is more suitable as the turbulence model because of the high accuracy of the RSM model to the swirl problem. A pressure-based transient solver is used, and the implicit formulation and Roe-FDS flux type are used to solve the problem. The governing equations, turbulent kinetic energy equations, and turbulent dissipation rate equations are calculated using the second-order upwind equation.

Pressure inlet and pressure outlet are used as boundary conditions, and there is no wall slip. When the research object is a supersonic separator, the coupling between the wall and the Eulerian liquid film model will be opened, to correctly handle the problem of droplet deposition and entrainment.

2.3. Model validation

Next, the model is validated, which can be mainly divided into two parts. Firstly, it is validated whether the model can accurately CO_2 condensation in a pure CO_2 system. Secondly, it is validated whether the evaluation of the overall performance and the prediction of the liquid film by the model are in place in the two-component system containing carrier gas.

Fig. 2 shows the structure and mesh of the supersonic nozzle being used to validate the pure CO_2 model. The structure and CO_2 condensation experiment carried out by this structure are from Lettieri et al. [49]. The total length of this nozzle is 98.37 mm, and the diameters of the inlet, throat, and outlet are 12.70 mm, 3.09 mm, and 4.01 mm respectively. A two-dimensional structured mesh is used and the area near the wall and throat is locally refined. Only half of the mesh is drawn, and the whole flow field is restored by choosing its axis as the axisymmetric boundary. To guarantee the accuracy of the mesh, a verification test is first performed. The Grid Convergence Index (GCI) is an estimate of the mesh refinement error derived based on the generalized ER

Table 2
The specific test results of the Grid Convergence Index.

			Grid a-b 1-fine 2-medium		**Grid b-c** 2-medium 3-coarse	
	F_s	p	$\varepsilon_{1,2}$ (%)	$GCI_{1,2}$ (%)	$\varepsilon_{2,3}$ (%)	$GCI_{2,3}$ (%)
Position	3	3	0.15 %	0.19 %	0.81 %	1.02 %

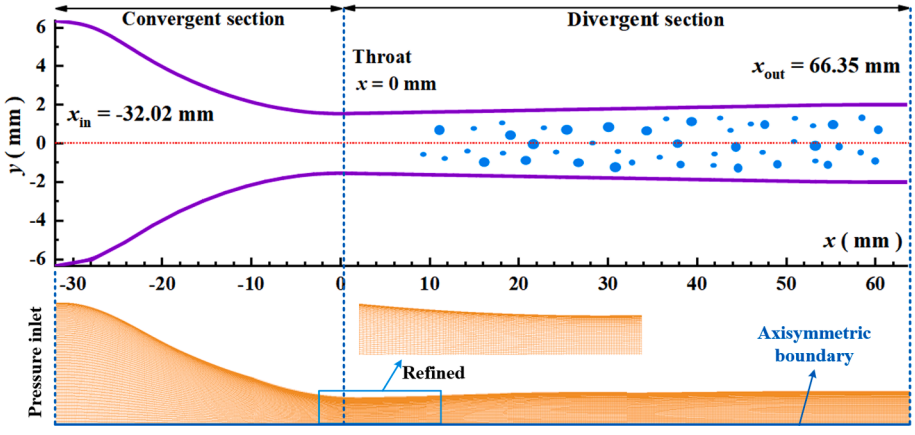

Fig. 2. The geometry and mesh of the supersonic nozzle.

extrapolation theory [50]. To obtain the best computational mesh, GCI was utilized to calculate and analyze three sets of meshes: a: fine (107,820 quad cells), b: medium (71,880 quad cells), and c: coarse (47,920 million quad cells). The calculation formula of GCI is as follows:

$$GCI = \frac{F_s|\varepsilon|}{\gamma^p - 1} \times 100\% \tag{23}$$

where F_s is the safety factor with an empirical parameter value of 3, ε is the relative error between the two grids, γ is the refinement factor ratio, and superscript p is the order of algorithm accuracy. Accurate prediction of condensation shockwave in a supersonic nozzle is a measure of grid quality. Taking the position of condensation shockwave as the parameter, the specific test results of GCI are shown in Table 2. The GCI value of Grid a-b is small and qualified, so the medium grid (71,880 elements) is selected, which improves the calculation speed and saves the calculation cost.

With the same pressure and temperature conditions as those in Lettieri's [49] experiment, namely, the inlet pressure is set to be p_{in} = 57.24 atm and the inlet temperature is set to be T_{in} = 314.78 K, a set of simulations are carried out using the established pure CO_2 model. The comparison between simulation results and experimental results is shown in Fig. 3. Fig. 3 (a) proves that the established pure CO_2 model has accuracy in predicting the position of the Wilson point when the real gas EOS is used. It is also obvious from the figure that when the ideal gas EOS is used, the nucleation position predicted by the model is later than that predicted by the real gas EOS, which leads to a deviation from the experimental values. In Fig. 3 (b), the prediction accuracy is further calculated, R Square (R^2) is used here to evaluate the consistency:

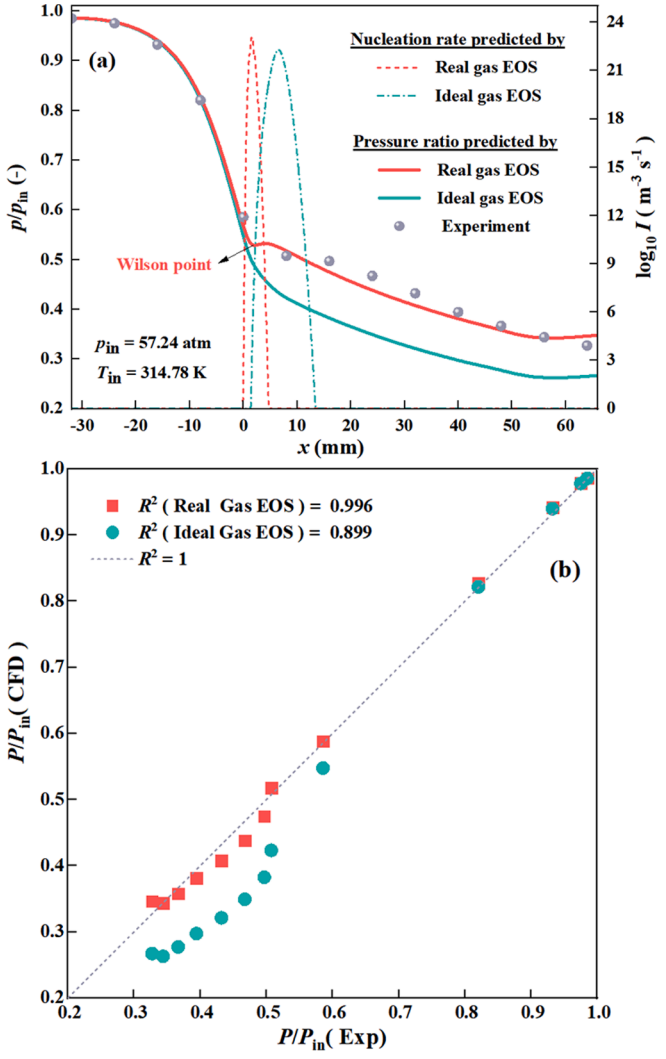

Fig. 3. Model validation: prediction of carbon condensation by Real gas EOS and Ideal gas EOS.

$$R^2 = 1 - \frac{\sum_{i=1}^{num}(a_i - b_i)^2}{\sum_{i=1}^{num}(a_i - \bar{a})^2} \tag{24}$$

where num, a_i, b_i, and $\bar{a}$ are the number of experimental points, experimental values, CFD values, and experimental sample mean value, respectively. It can also be seen intuitively from the figure that R^2 (Real gas EOS) of the pressure ratio can reach 0.996, but R^2 (Ideal gas EOS) of the pressure ratio is only 0.899, therefore, the established pure CO_2 model can be used to simulate the carbon condensation in supersonic nozzles, especially after considering the real gas EOS.

The main purpose of the second validation is to validate the prediction effect of the model on the separation performance of the two-component system. The research object is the supersonic separator shown in Fig. 4. At present, the experiment of CO_2 condensation and separation of the two-component system in the supersonic separator is still blank, so we use our equipment to experiment on an air–steam system. The experimental device and method were introduced in detail in our previous work [40]. Under the experimental conditions, the inlet pressure and outlet pressure are 3 atm and 1 atm respectively, the inlet temperature and outlet temperature are 300 K, the inlet humidity is 100 %, and the diameter and mass concentration of heterogeneous droplets at the inlet are 2.2 μm and 0.005 kg/m^3 respectively.

Similarly, the simulation keeps the same conditions as the experiment, and the three-dimensional structured mesh used in the simulation is shown in Fig. 4. By conducting GCI tests, the number of grid cells was determined to be 557,560. Fig. 5(a) shows the comparison between the experimental results and the simulation results. Dew point depression ΔT_d and vapour separation efficiency η_v are parameters used to evaluate separation performance, and their calculation methods are as follows:

$$\Delta T_d = T_{d,\,in} - T_{d,\,out} \tag{25}$$

$$\eta_v = \frac{y_{v,\,in} - y_{v,\,out}}{y_{v,\,in}} \times 100\% \tag{26}$$

where $T_{d,\,in}$ and $T_{d,\,out}$ are the dew point at the inlet and gas outlet, $y_{v,\,in}$ and $y_{v,\,out}$ are the vapour mole fraction at the inlet and gas outlet. ΔT_d obtained by experiment and CFD are 20.04 K and 22.95 K, respectively, and η_v captured by experiment and CFD are 73.04 % and 77.27 % respectively. The relative errors are 12.67 % and 5.47 %, which is within the acceptable range. The agreement between them is great, which proves that the established model can calculate the separation performance well. In addition, three cases of CFD and experiments of liquid film thickness are compared. The difference between the three cases is that the mass concentration of heterogeneous droplets at the inlet is 0.0001 kg/m^3, 0.0010 kg/m^3 and 0.0020 kg/m^3 respectively. Fig. 5(b) is the comparison between the experiment and CFD. For the three cases, the experimental film thicknesses at the liquid outlet are 18.80 μm, 52.71 μm, and 89.24 μm, respectively, while the CFD film thicknesses are 12.74 μm, 50.29 μm, and 88.15 μm, respectively. Fig. 5(c) shows the change of film thickness at the liquid outlet of the three cases within 120 s during the experiment, when the liquid film is thin, the deviation between the experiment and CFD results is slightly larger, which is because the flow fluctuation at the actual liquid outlet is more complicated and more difficult to observe, but generally speaking, the deviation between the experiment and CFD is within a reasonable range. To sum up, the established model is practical and can be used as the basis for further research.

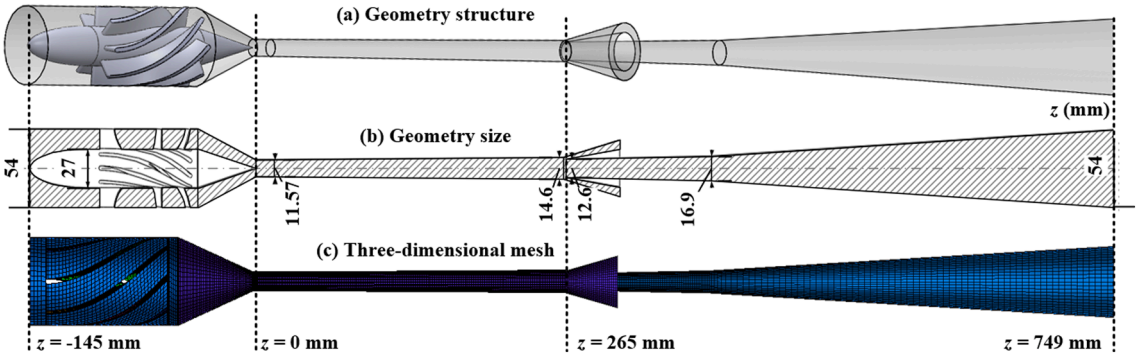

Fig. 4. Structure, size, and mesh of the supersonic separator.

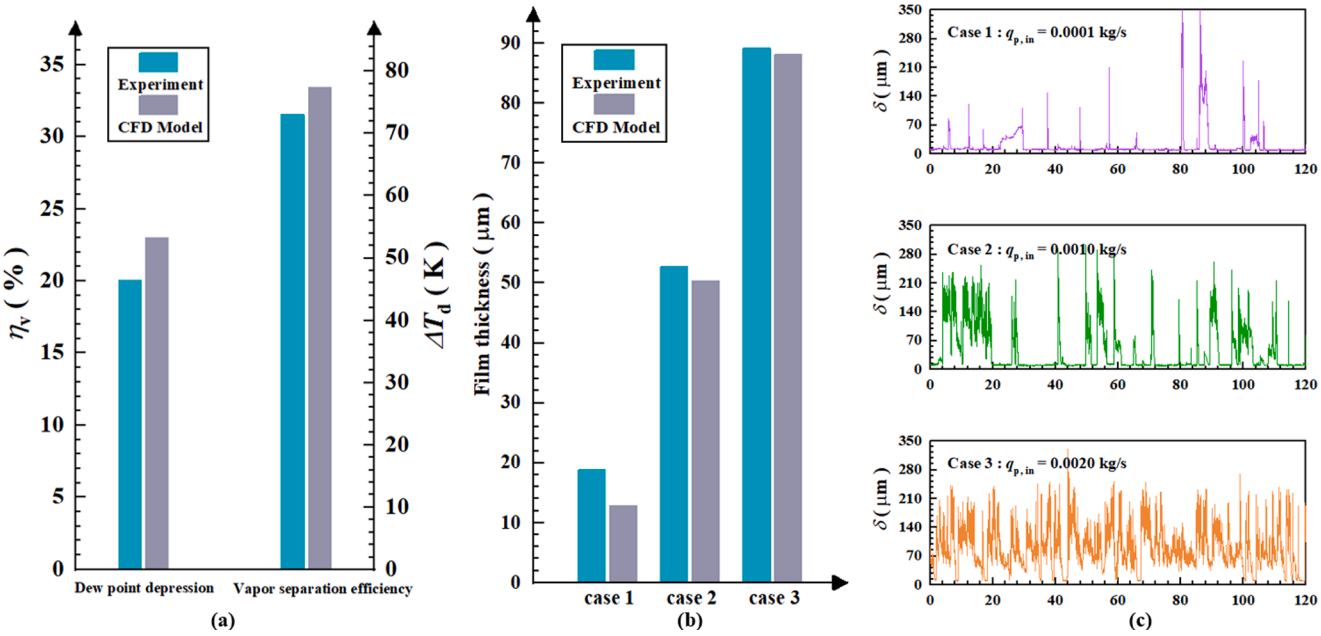

Fig. 5. Model validation: prediction of condensation and separation performance.

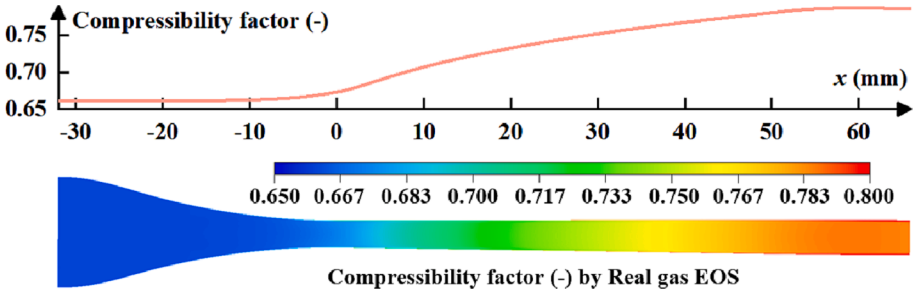

Fig. 6. Compressibility factor of Real gas EOS model in supersonic flow.

3. Results and discussion

3.1. Evaluation of condensation performance

Taking the supersonic nozzle (Fig. 2) as the research object, using the pure CO_2 model, different thermodynamic models are compared, the condensation mechanism of carbon dioxide is illustrated, and the environment easy to condense is pointed out. Using the CH_4-CO_2 model, the effects of different conditions on CO_2 condensation are studied.

3.1.1. CO_2 condensation flow predicted by thermodynamic models

Firstly, different thermodynamic models are compared. Fig. 6 shows the profile of the compressibility factor of the pure CO_2 model considering the real gas EOS. The compressibility factor is usually considered an indicator of deviation from the ideal gas hypothesis. The compressibility factor ranges from 0.65 at the supersonic nozzle inlet to 0.80 at the nozzle outlet, which indicates that an ideal gas EOS can lead to inaccurate prediction of heat and fluid flow in supersonic flow. Fig. 7 is a comparison diagram of properties predicted by real gas EOS and ideal gas EOS under different conditions, the specific simulation conditions

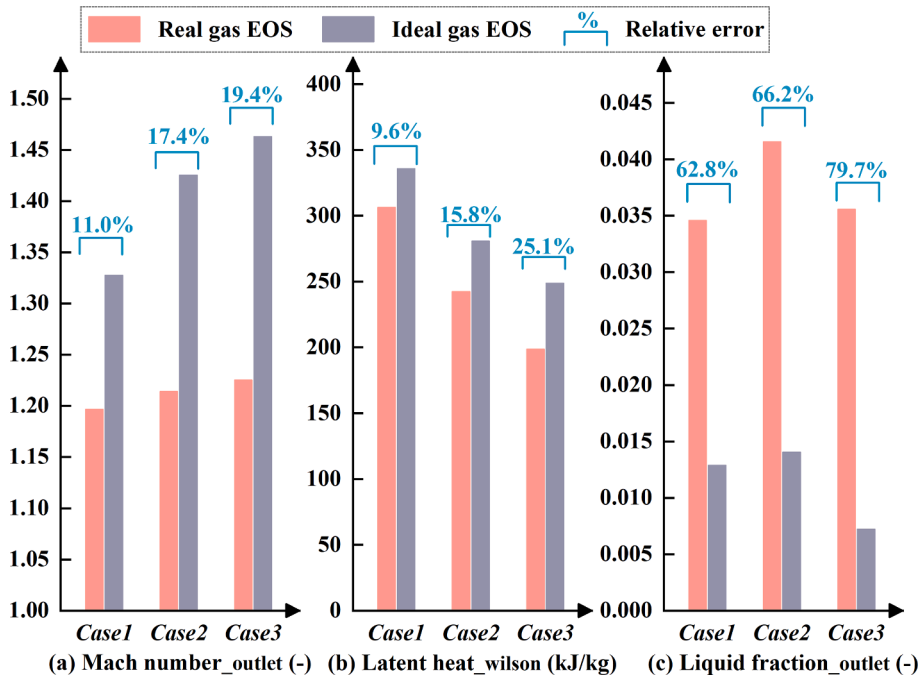

Fig. 7. Prediction properties of thermodynamic models in supersonic flow under different conditions.

Table 3
Simulation conditions for pure CO_2 model.

Case	p_{in} (atm)	p_{out} (atm)	T_{in} (K)	T_{out} (K)	T_{sat} (K)	ΔT_{in} (K)	State
Case 1	30	10	278	300	268	−10	subcritical
Case 2	60	10	310	300	295	−5	near-critical
Case 3	100	10	340	300	304	−26	supercritical

are shown in Table 3. As shown in Fig. 7 (a), the relative error between ideal gas EOS and real gas EOS in predicting the Mach number of nozzle outlet in *Case 1* with the subcritical state is 11.0 %, which means that the ideal gas hypothesis overestimates the expansion characteristics of carbon dioxide in the supersonic nozzle. Besides, when predicting *Case 2* and *Case 3*, the relative error climbed to 17.4 % and 19.4 %, indicating that the increase in pressure will magnify this overestimation. Fig. 7 (b) shows the release of latent heat at Wilson point. Similarly, the ideal gas EOS overestimates the heat transfer characteristics of CO_2 condensation, and with the increase of pressure, this overestimation is enlarged from 9.6 % to 25.1 %. Fig. 7 (c) shows the liquid fraction at the nozzle outlet predicted by different thermodynamic models. The ideal gas EOS seriously underestimates this value, which proves that its grasp of mass transfer characteristics is also very inaccurate. For example, in *Case 3*

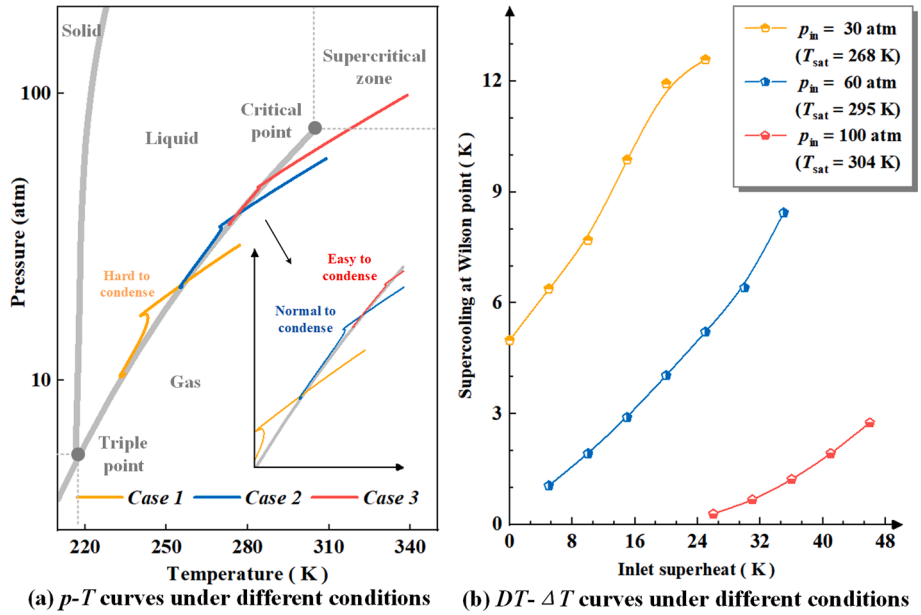

Fig. 8. *p-T* and *DT-ΔT* curves under different conditions for non-equilibrium condensation.

with supercritical state, the predicted liquid fraction at the nozzle outlet of the real gas EOS is 0.03557, while the predicted value by the ideal gas EOS is only 0.00723, with a dramatic relative error of 79.7 %. Compared with the ideal gas EOS, the real gas EOS is more suitable for the prediction of expansion characteristics and mass-heat transfer in supersonic condensation flow, and the increase of pressure environment will enlarge the deviation between the ideal gas EOS and the real value.

Then, the *p-T* curves of real gas EOS with a more accurate description of the flow field under the three conditions are observed and plotted in Fig. 8 (a). It can be seen intuitively from this figure that when the pressure is in the subcritical state, it still takes a long time to struggle to reach the condensation condition after CO_2 gas reaches gas–liquid saturation. When the pressure rises to the near-critical state, condensation becomes a little easier, and when the pressure rises to the supercritical state, condensation happens almost as soon as it touches the saturation line. Keeping the pressure constant, a series of simulations of varying inlet superheat *DT* (negative supercooling) are conducted and the supercooling at the Wilson point of each case is collected, as shown in Fig. 8 (b). When the gas pressure at the inlet is relatively high, the supercooling at Wilson point will be relatively small, that is, the temperature drop required to reach the condensation condition will be relatively small, and condensation will occur more easily.

3.1.2. Condensing CO_2 nanodroplets from natural gas

In the previous section, the result that CO_2 is easier to condense in a high-pressure environment has been discussed. In this section, the influence of different conditions on CO_2 condensation of carbon-rich natural gas in a high-pressure is concerned. Unless otherwise specified, the thermodynamic model will always use the real gas EOS from this section onwards. Set the inlet pressure as $p_{in} = 80$ atm, outlet pressure as $p_{out} = 20$ atm, inlet CO_2 vapour mole fraction as $y_{CO2,in} = 25$ %, and the effect of inlet temperature on condensation is summarized in Fig. 9. Fig. 9 (a)- Fig. 9 (d) are the distributions of droplet radius, supercooling, nucleation rate, and vapour mole fraction of the flow field in the supersonic nozzle when T_{in} is changed. Correspondingly, Fig. 9 (e)- Fig. 9 (h) are line charts of data distribution on its axis. It can be found that with the increase in temperature, the radius of the condensed CO_2 nanodroplets at the outlet decrease from 0.44 μm to 0.29 μm, the condensation onset position (Wilson point) moves backwards, and the supercooling at Wilson point increases by 4.53 K. The nucleation position moved backwards by 43.8 mm, and the nucleation range and outlet mole fraction also decrease. Keep the inlet pressure at 80 atm, the outlet pressure at 20 atm, and the inlet temperature at 273 K, and increase the vapour mole fraction of CO_2. This is because the higher the inlet temperature, the greater the supercooling required for condensation, and the condensation is more difficult to achieve. Fig. 10 are cloud maps and axial distributions of condensation properties of CO_2 under different inlet CO_2 vapour mole fractions. It can be found that with the increase of inlet carbon dioxide mole fraction, the condensation onset position moves forward, and the supercooling at Wilson point decreases by 12.09 K. The radius of the condensed droplets at the outlet decreases by 0.07 μm. The nucleation position moved forward by 39.8 mm. This is because the greater the inlet CO_2 vapour mole fraction, the greater the partial pressure of CO_2 in the gas mixture, the easier it is for CO_2 to condense, and the more CO_2 will condense.

The condensation amount of CO_2 under different conditions is calculated and shown in Fig. 11. Here, the condensation amount is evaluated by two indexes: the condensed mole fraction of CO_2 (y_{con}) and the condensed CO_2 mass per hour $\dot{m}_{con}$ (ton/h), namely

$$\begin{cases} y_{con} = \dfrac{y_{CO_2,in} - y_{CO_2,out}}{y_{CO_2,in}} \\ \dot{m}_{con} = \dfrac{Y_{CO_2,in}\dot{m}_{in} - Y_{CO_2,out}\dot{m}_{out}}{3.6} \end{cases} \tag{27}$$

where $\dot{m}_{in}$ and $\dot{m}_{out}$ are the mass flow rate (kg s^{-1}) at the nozzle inlet and outlet. It can be seen from Fig. 11 that when the inlet temperature rises, y_{con} and $\dot{m}_{con}$ show a downward trend. When the inlet temperature rises from 263 K to 283 K, y_{con} and $\dot{m}_{con}$ decrease from 19.47 % and 10.33 ton/h to 7.84 % and 2.84 ton/h respectively. On the contrary, when $y_{CO2,in}$ increases, y_{con} and $\dot{m}_{con}$ both increase significantly. With the increase of $y_{CO2,in}$ from 20 % to 35 %, y_{con} and $\dot{m}_{con}$ increased from 13.22 % and 4.41 ton/h to 17.53 % and 11.67 ton/h, respectively. Lowering the inlet temperature or increasing the inlet vapour mole fraction can be used as means to improve the carbon condensation performance and contribute to the development of supersonic decarbonization technology.

3.2. Evaluation of separation performance

Taking the supersonic separator (Fig. 4) as the research object, using the CH_4-CO_2 model, the separation processes dominated by homogeneous condensation and heterogeneous condensation are studied respectively, and the separation amount was evaluated.

3.2.1. Separation process dominated by homogeneous condensation

The cloud chart shown in Fig. 12 shows the behaviour characteristics of vapour, droplets, and liquid film in the supersonic separator when

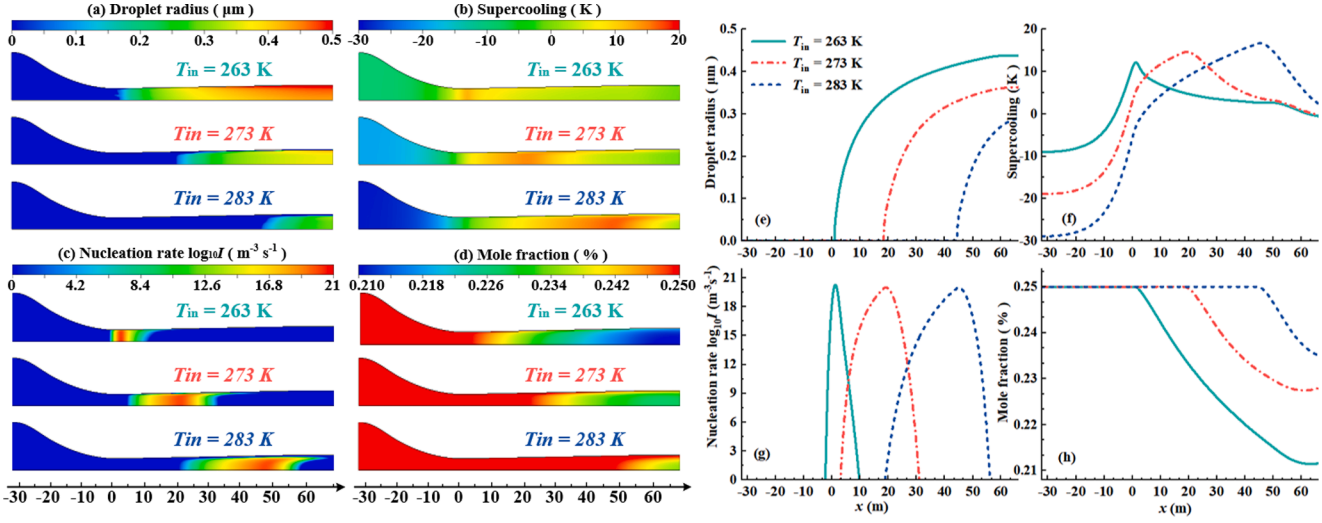

Fig. 9. The effect of inlet temperature on CO_2 condensation.

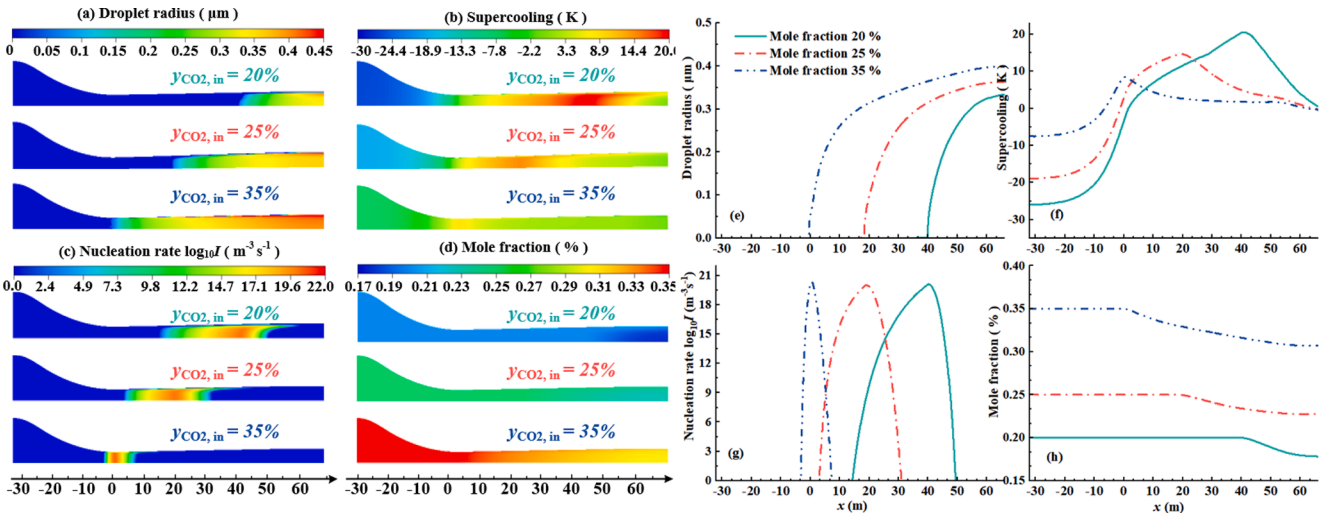

Fig. 10. The effect of inlet CO_2 vapour mole fraction on CO_2 condensation.

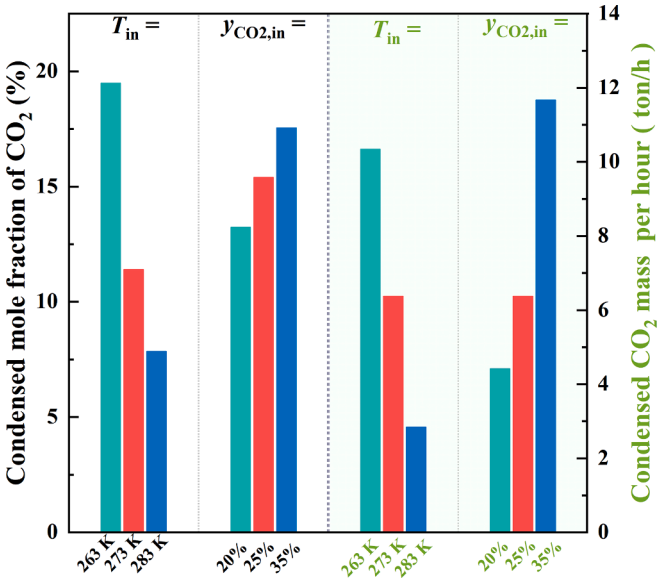

Fig. 11. Condensation amount of CO_2 under different conditions.

only homogeneous condensation exists. The simulated inlet conditions are $p_{in} = 150$ atm, $T_{in} = 258$ K, $y_{CO2,\ in} = 23.2$ %, gas outlet condition is $p_{g,out} = 80$ atm, liquid outlet condition is $p_{l,out} = 60$ atm. As can be seen from Fig. 12 (a), the CO_2 vapour undergoes the process of firstly condensation and then evaporation in the supersonic separator, and its mole fraction can be reduced to 0.13 at the lowest. As shown in Fig. 12 (b), the condensation process will produce homogeneous CO_2 droplets, the size of which is very small, and the largest droplet has a radius of 1.35 μm. Under the action of swirling flow, the CO_2 droplets will be thrown to the wall to form the liquid film. However, due to the small particle size of homogeneous droplets, they are more likely to be entrained by the gas phase, instead of forming the wall film. The liquid film shown in Fig. 12 (c) has only a very thin layer, and the maximum thickness is only 1.10 μm. The reason for its formation is the condensation of CO_2 vapour near the wall and the deposition of a few CO_2 droplets. Fig. 13 shows the proportion of different forms of carbon dioxide in the supersonic separator of this case, all the data come from the axis. It can also be seen from the figure that the mole fraction of CO_2 vapour at the inlet and outlet of the supersonic separator is almost equal, which indicates that the separation amount of the separation process dominated by homogeneous condensation approaches zero.

3.2.2. *Separation process dominated by heterogeneous condensation*

Next, the separation process dominated by heterogeneous condensation is discussed. Keeping the above simulation conditions unchanged, heterogeneous droplets with a radius of 10 μm and a mass concentration of $\rho_{het,in} = 7.5$ kg/m^3 are continuously injected into the inlet, and the changes of gas, droplet, and liquid film are shown in Fig. 14. It can be seen that, compared with Fig. 12, the lowest value of the mole fraction of CO_2 vapour can be reduced to 0.10, and the particle size of homogeneous droplets can also be increased to 1.62 μm. At the throat, homogeneous droplets will collide with heterogeneous droplets, and be aggregated into heterogeneous droplets with larger particle sizes. When the heterogeneous droplet is the largest, the particle size can grow to about 0.1 mm, which means that it can provide more opportunities for vapour condensation. The separation process is completed when the liquid film on the wall flows out of the liquid outlet. Therefore, more liquid film content is beneficial to separation. When heterogeneous droplets exist, the number of large droplets in the flow field significantly increases, so the number of droplets that can be thrown to the wall surface increases. As shown in Fig. 14 (d), the liquid film thickness of this case ranges from 13 μm to 121 μm, which means better separation capacity.

Fig. 15 is the influence of different heterogeneous droplet mass concentrations on the molar fraction of CO_2 vapour. It is easy to conclude that when $\rho_{het,in}$ increases, the mole fraction of CO_2 vapour at the outlet will decrease, which means that more CO_2 vapour is separated in the form of the liquid phase. For example, when $\rho_{het,in} = 0.1$ kg/m^3, the mole fraction of CO_2 vapour at the outlet is 19.4 %, and when $\rho_{het,in} = 7.5$ kg/m^3, this value decreases to 15.9 %.In the diffuser, the mole fraction of carbon dioxide vapour rises. This is because the pressure rise in the diffuser is accompanied by the temperature rise, which creates conditions for the evaporation of droplets. Fig. 16 is the energy and mass evaluation of different $\rho_{het,in}$, as can be seen from Fig. 16 (a) and Fig. 16 (b), when $\rho_{het,in}$ increases from 0.1 kg/m^3 to 7.5 kg/m^3, y_{con} and $\dot{m}_{con}$ increase from 6.73 % and 3.33 ton/h to 23.53 % and 4.43 ton/h, respectively. This is because when the concentration of heterogeneous droplets increases, it means that there are more condensable cores in the flow field, which provides more opportunities for the accumulation and condensation of CO_2 vapour, and the condensed CO_2 will grow more fully, which also indicates that more mass of CO_2 will be separated in the form of droplets. Fig. 16 (c) counts the exergy loss per kg condensed CO_2 under different $\rho_{het,in}$. When $\rho_{het,in}$ changed from 0.1 kg/m^3 to 7.5 kg/m^3, the value of exergy loss dropped from 436.57 kJ/kg to 329.56 kJ/kg,

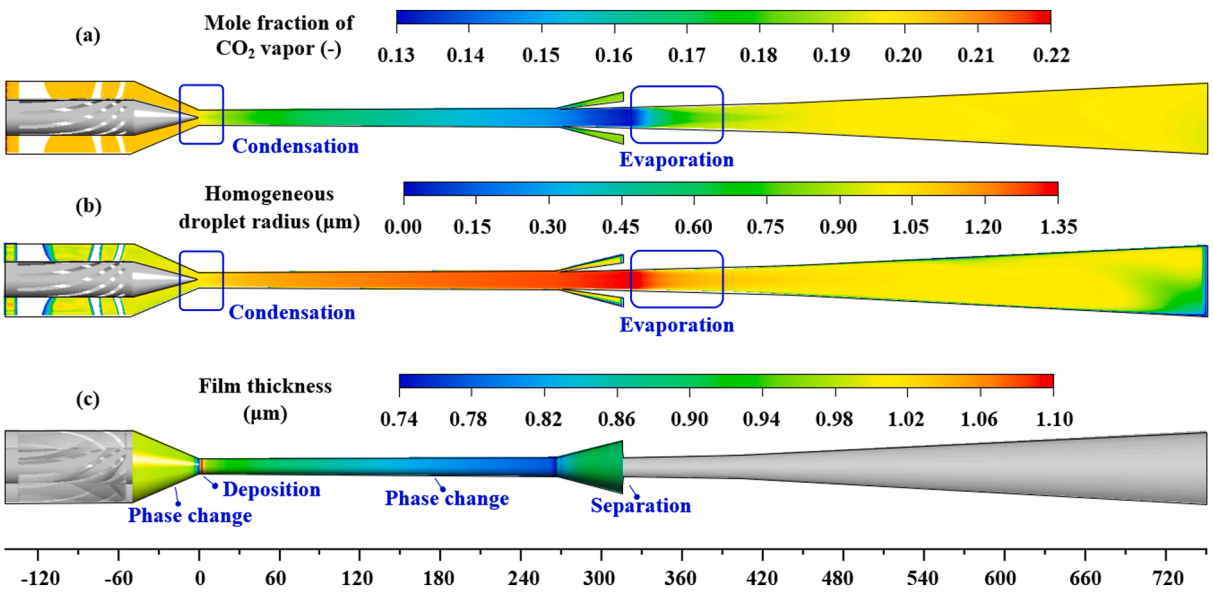

Fig. 12. Behavior of gas, liquid droplets, and liquid film in supersonic separator dominated by homogeneous condensation.

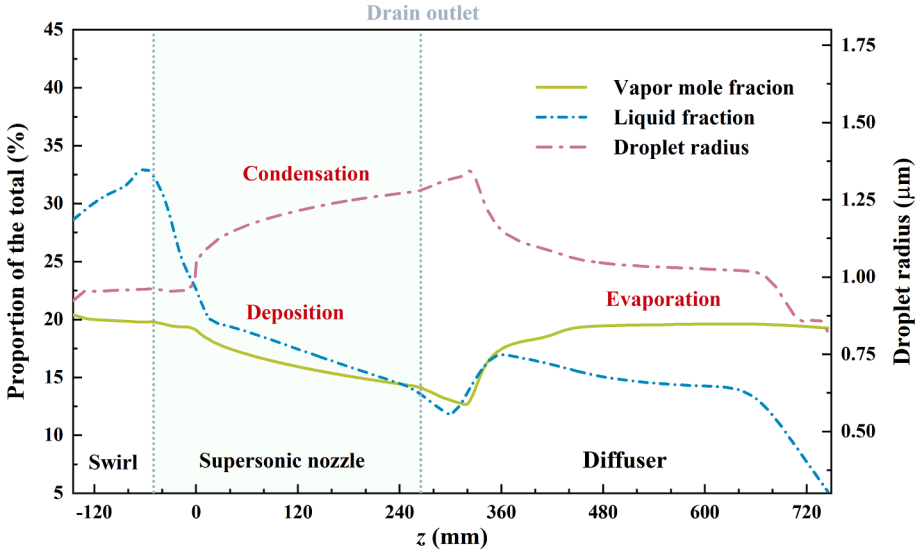

Fig. 13. The proportion of different forms of carbon dioxide.

this shows that when the concentration of foreign core is relatively large, the exergy required for condensation will decrease. Generally speaking, the increase of heterogeneous droplet concentration, that is, the increase of heterogeneous cores, can have a positive impact on the mass collection and energy utilization in the CO_2 condensation process, and can be used as an effective means to strengthen the performance of the supersonic separator.

3.3. Discussion

In this paper, the brand-new CCUS technology, namely the concept of supersonic separation, which can provide a new way for decarbonization, is systematically studied. The implementation of this research can provide positive help for the treatment and purification of offshore natural gas. Offshore gas wells used for natural gas production are heavy carbon emitters, and tens of thousands of tons of carbon dioxide are discharged as by-products of natural gas exploitation every year. The new concept described in this paper separates and produces liquefied carbon dioxide from a high-pressure supersonic separator, and it can be commercialized by dew point adjustment [51]. Compared with conventional methods, the core of offshore natural gas treatment by supersonic decarbonization lies in the Laval nozzle in the tubular device to ensure the supersonic flow of non-equilibrium condensation of condensable parts. This simple structure and the pollution-free way can win the potential for the new method to make the natural gas plant have higher income, lower operating cost, and more environmental sustainability.

One of the contributions of this paper is the hope to promote the deep development of this field and achieve a win–win balance between energy and the environment. A model considering gas, liquid droplets, liquid film, condensation, swirl, slip, collision, and coalescence is established to evaluate the applicability of supersonic decarbonization. The prediction accuracy of this model for condensation performance keeps a high correlation with the near-critical experiment of Lettieri et al.[49], while the prediction of separation efficiency and the liquid film is proved to be accurate by a gas–water separation experiment. This is due to the compromise of the lack of high-pressure experimental data. For the development and application of the supersonic decarbonization

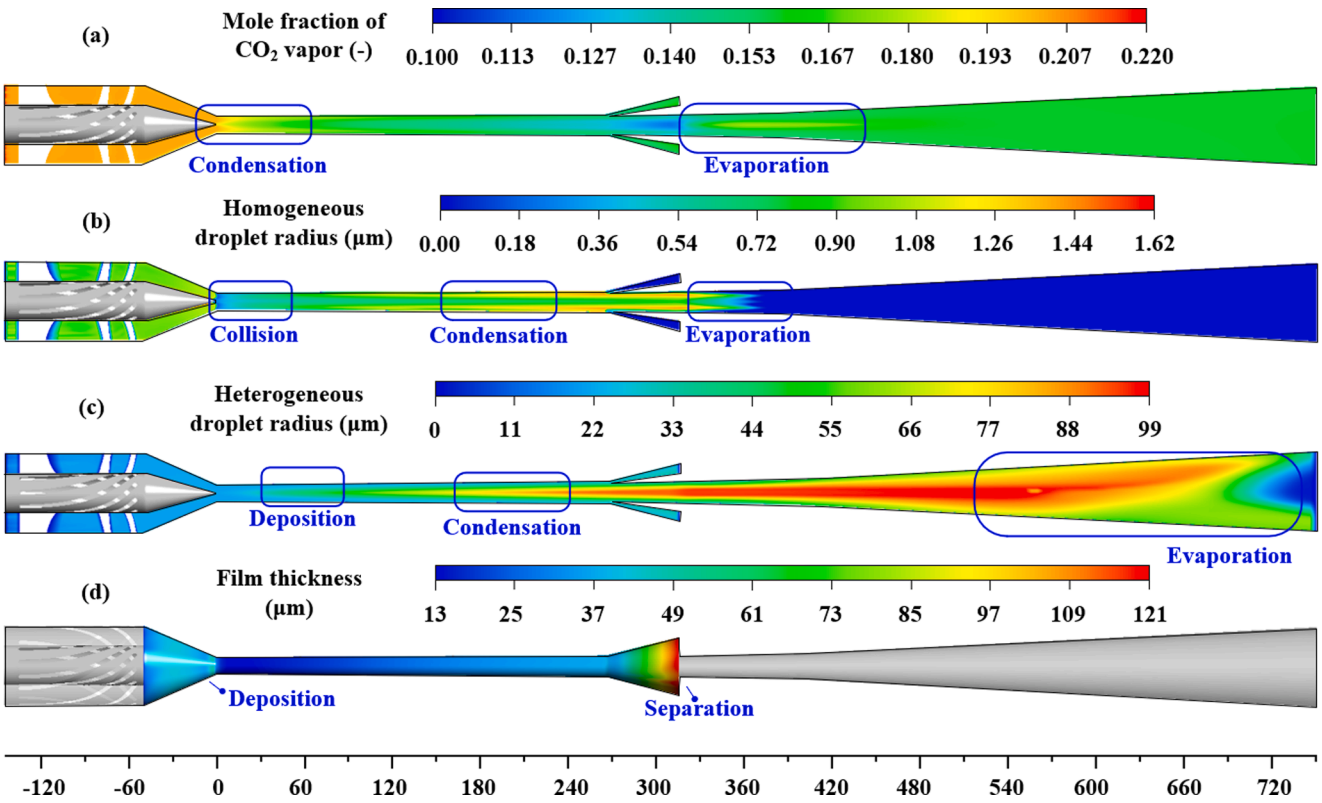

Fig. 14. Behavior of gas, liquid droplets, and liquid film in supersonic separator dominated by heterogeneous condensation.

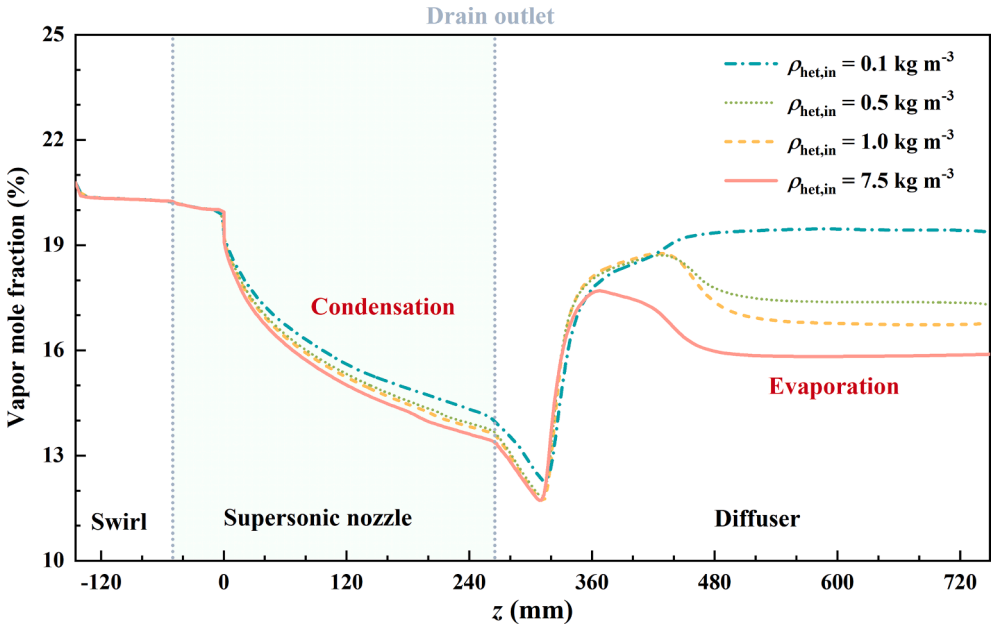

Fig. 15. The effects of different heterogeneous droplet mass concentrations on CO_2 vapour molar fraction.

method, in the foreseeable future, it is hoped that there will be more experimental methods and the resulting data, which can be deeply bound with the numerical simulation results. The pressure distribution, droplet size, liquid fraction, and gas humidity of supersonic equipment in the process of high-pressure carbon dioxide condensation should be paid attention to fill the data gaps in this respect.

The research in this paper points out a direction for the operation conditions of supersonic decarbonization equipment, and the follow-up work can continue to dig along the direction of high pressure, low temperature, and high heterogeneous droplet mass concentration to determine a more accurate operation condition. In addition, regarding the condensation and separation performance, besides the difference in conditions, the structure of the equipment will also have a significant impact. In this paper, the supersonic nozzle structures used in Fig. 2 and Fig. 4 are different, and the condensation performances obtained by simulation are also different. It is appropriate for further work to focus on exploring low-cost and high-efficiency supersonic separation structures, which may require a complex combination of theoretical analysis,

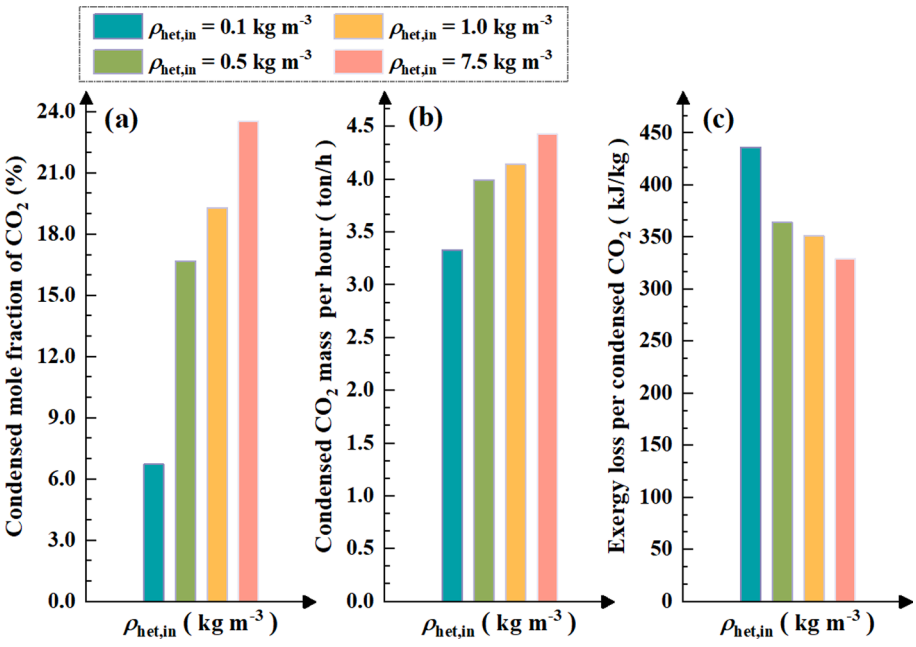

Fig. 16. Energy and mass evaluation of different heterogeneous droplet mass concentration.

experimental basis, and computational science.

4. Conclusion

A computational fluid dynamics model considering the complex physical characteristics of the supersonic decarbonization concept is established and validated to evaluate the pioneering contribution of this new concept to CCUS technology. High-pressure operating conditions closer to actual production and real gas EOS are selected as part of the model. The established model is compatible with the pure CO_2 model and CH_4-CO_2 model and has been applied to two research objects, a supersonic nozzle and a supersonic separator, for evaluating the condensation and separation performance of the supersonic decarbonization concept. The integrated conclusions of the evaluation results are as follows:

i. Compared with the ideal gas EOS, the real gas EOS is more suitable for the prediction of expansion characteristics and mass-heat transfer in supersonic condensation flow, and the increase of pressure environment will enlarge the deviation between the ideal gas EOS and the real value.
ii. Higher pressure will make the properties of carbon dioxide develop into a state of easy condensation. Keep p_{in} at a supercritical state, with T_{in} increases from 263 K to 283 K, the radius of the condensed CO_2 nanodroplets at the outlet decrease from 0.44 μm to 0.29 μm, the Wilson point moves backwards, the supercooling at Wilson point increases by 4.53 K, and y_{con} and $\dot{m}_{con}$ decrease from 19.47 % and 10.33 ton/h to 7.84 % and 2.84 ton/h.
iii. Keep p_{in} at a supercritical state, with $y_{CO2,in}$ increases from 20 % to 35 %, the Wilson point moves forward, and the supercooling at Wilson point decreases by 12.09 K. The radius of the condensed droplets at the outlet decreases by 0.07 μm, while y_{con} and $\dot{m}_{con}$ increase from 13.22 % and 4.41ton/h to 17.53 % and 11.67 ton/h.
iv. The separation amount of the separation process dominated by homogeneous condensation approaches zero. When a certain mass concentration of heterogeneous droplets is added at the inlet, the separation effect is improved. When $\rho_{het,in}$ increases from 0.1 kg/m^3 to 7.5 kg/m^3, y_{con} and $\dot{m}_{con}$ increase from 6.73 % and 3.33 ton/h to 23.53 % and 4.43 ton/h, respectively.
v. When $\rho_{het,in}$ increases from 0.1 kg/m^3 to 7.5 kg/m^3, exergy loss per kg condensed CO_2 dropped from 436.57 kJ/kg to 329.56 kJ/kg, this shows that when the concentration of foreign core is relatively large, the exergy required for condensation will decrease.

The precision of operation conditions, the determination of optimal structure, and the implementation of the high-pressure experiments will be the focus of the follow-up work.

CRediT authorship contribution statement

Hongbing Ding: Conceptualization, Supervision, Funding acquisition, Investigation, Methodology, Writing - original draft, Writing - review & editing. **Yu Zhang:** Formal analysis, Investigation, Writing - original draft, Writing - review & editing. **Yuanyuan Dong:** Methodology, Writing - review & editing. **Chuang Wen:** Formal analysis, Methodology, Conceptualization, Funding acquisition, Writing - review & editing. **Yan Yang:** Supervision, Visualization, Methodology, Funding acquisition, Writing - review & editing.

Declaration of Competing Interest

The authors declare that they have no known competing financial interests or personal relationships that could have appeared to influence the work reported in this paper.

Data availability

The research data supporting this publication are provided within this paper.

Acknowledgement

This work is supported in part by the National Natural Science Foundation of China under Grants 52276159, 51876143 and 62073135, the Engineering and Physical Sciences Research Council [grant number EP/X027147/1]. For the purpose of open access, the author has applied a ‘Creative Commons Attribution (CC BY) licence to any Author Accepted Manuscript version arising.

References

[1] Wang Q, Pfeiffer H, Amal R, O'Hare D. Introduction to CO2 capture, utilization and storage (CCUS). React Chem Eng 2022;7(3):487–9.
[2] Zhang Z, Wang T, Blunt MJ, Anthony EJ, Park A-H, Hughes RW, et al. Advances in carbon capture, utilization and storage. Appl Energ 2020;278:115627.
[3] Karasu S, Altan A. Crude oil time series prediction model based on LSTM network with chaotic Henry gas solubility optimization. Energy 2022;242:122964.
[4] Yan J, Zhang Z. Carbon Capture, Utilization and Storage (CCUS). Appl Energ 2019; 235:1289–99.
[5] Jia B, Tsau J, Barati R. A review of the current progress of CO2 injection EOR and carbon storage in shale oil reservoirs. Fuel 2019;236:404–27.
[6] Kim TH, Cho J, Lee KS. Evaluation of CO2 injection in shale gas reservoirs with multi-component transport and geomechanical effects. Appl Energ 2017;190: 1195–206.
[7] Chu F, Yang L, Du X, Yang Y. Mass transfer and energy consumption for CO2 absorption by ammonia solution in bubble column. Appl Energ 2017;190:1068–80.
[8] Zhang Z, Cai J, Chen F, Li H, Zhang W, Qi W. Progress in enhancement of CO2 absorption by nanofluids: A mini review of mechanisms and current status. Renew Energ 2018;118:527–35.
[9] Koronaki IP, Prentza L, Papaefthimiou V. Modeling of CO2 capture via chemical absorption processes – An extensive literature review. Renew Sustain Energy Rev 2015;50:547–66.
[10] Zhao R, Zhao Li, Deng S, Song C, He J, Shao Y, et al. A comparative study on CO2 capture performance of vacuum-pressure swing adsorption and pressure-temperature swing adsorption based on carbon pump cycle. Energy 2017;137: 495–509.
[11] Chaffee AL, Knowles GP, Liang Z, Zhang J, Xiao P, Webley PA. CO2 capture by adsorption: Materials and process development. Int J Greenh Gas Con 2007;1(1): 11–8.
[12] Petrovic B, Gorbounov M, Masoudi Soltani S. Impact of Surface Functional Groups and Their Introduction Methods on the Mechanisms of CO2 Adsorption on Porous Carbonaceous Adsorbents. Carbon Capture Sci Technol 2022;3:100045.
[13] Brunetti A, Scura F, Barbieri G, Drioli E. Membrane technologies for CO2 separation. J Membrane Sci 2010;359(1-2):115–25.
[14] Castro-Muñoz R, Zamidi Ahmad M, Malankowska M, Coronas J. A new relevant membrane application: CO2 direct air capture (DAC). Chem Eng J 2022;446: 137047.
[15] Yamasaki H, Wakimoto H, Kamimura T, Hattori K, Neksa P, Yamaguchi H. Visualization and Measurement of Swirling Flow of Dry Ice Particles in Cyclone Separator-Sublimator. Energies 2022;15:4128.
[16] Song C, Liu Q, Deng S, Li H, Kitamura Y. Cryogenic-based CO2 capture technologies: State-of-the-art developments and current challenges. Renew Sustain Energy Rev 2019;101:265–78.
[17] Wen C, Karvounis N, Walther JH, Yan Y, Feng Y, Yang Y. An efficient approach to separate CO2 using supersonic flows for carbon capture and storage. Appl Energ 2019;238:311–9.
[18] Ding H, Zhang Yu, Yang Y, Wen C. A modified Euler-Lagrange-Euler approach for modelling homogeneous and heterogeneous condensing droplets and films in supersonic flows. Int J Heat Mass Tran 2023;200:123537.
[19] Niknam PH, Mortaheb HR, Mokhtarani B. Optimization of dehydration process to improve stability and efficiency of supersonic separation. J Nat Gas Sci Eng 2017; 43:90–5.
[20] Arinelli LDO, Trotta TAF, Teixeira AM, de Medeiros JL, Araújo ODQF. Offshore processing of CO2 rich natural gas with supersonic separator versus conventional routes. J Nat Gas Sci Eng 2017;46:199–221.
[21] Gonzaga CSB, Arinelli LdO, de Medeiros JL, Araújo OdQF. Automatized Monte-Carlo analysis of offshore processing of CO2-rich natural gas: Conventional versus supersonic separator routes. J Nat Gas Sci Eng 2019;69:102943.
[22] Jiang W, Bian J, Wu A, Gao S, Yin P, Hou D. Investigation of supersonic separation mechanism of CO2 in natural gas applying the Discrete Particle Method. Chem Eng Process - Process Intesif 2018;123:272–9.
[23] Gerber AG, Kermani MJ. A pressure based Eulerian-Eulerian multi-phase model for non-equilibrium condensation in transonic steam flow. Int J Heat Mass Tran 2004; 47(10-11):2217–31.
[24] Zudin. Non-equilibrium evaporation and condensation processes. Springer International Publishing; 2019.
[25] Lv X, Bai B. A multi-fluid model for non-equilibrium condensation in gaseous carrier flows. Appl Therm Eng 2014;65(1-2):24–33.
[26] Castier M. Modeling and simulation of supersonic gas separations. J Nat Gas Sci Eng 2014;18:304–11.
[27] Chen J, Jiang W, Han C, Liu Y. Numerical study on the influence of supersonic nozzle structure on the swirling condensation characteristics of CO2. J Nat Gas Sci Eng 2021;88:103753.
[28] Niknam PH, Mortaheb HR, Mokhtarani B. Effects of fluid type and pressure order on performance of convergent–divergent nozzles: An efficiency model for supersonic separation. Asia Pac J Chem Eng 2018;13(2):e2181.
[29] Wen C, Li Bo, Ding H, Akrami M, Zhang H, Yang Y. Thermodynamics analysis of CO2 condensation in supersonic flows for the potential of clean offshore natural gas processing. Appl Energ 2022;310:118523.
[30] Ding H, Dong Y, Zhang Yu, Yang Y, Wen C. A potential strategy of carbon dioxide separation using supersonic flows. Sep Purif Technol 2022;303:122153.
[31] Chen J, Huang Z, Jiang W. Non-equilibrium condensation of carbon dioxide in flue gas with the coexistence of swirl flows and supersonic flows. Int Commun Heat Mass 2022;138:106369.
[32] Yue Ti, Chen J, Song J, Chen X, Wang Y, Jia Z, et al. Experimental and numerical study of Upper Swirling Liquid Film (USLF) among Gas-Liquid Cylindrical Cyclones (GLCC). Chem Eng J 2019;358:806–20.
[33] Li H, Anglart H. Prediction of dryout and post-dryout heat transfer using a two-phase CFD model. Int J Heat Mass Tran 2016;99:839–50.
[34] Chen W, Chen Y, Zhang W, He S, Li B, Jiang J. Paint thickness simulation for robotic painting of curved surfaces based on Euler-Euler approach. J Braz Soc Mech Sci 2019;41:1–9.
[35] Ding H, Sun C, Wen C, Liang Z. The droplets and film behaviors in supersonic separator by using three-field two-fluid model with heterogenous condensation. Int J Heat Mass Tran 2022;184:122315.
[36] Deng Q, Jiang Y, Hu Z, Li J, Feng Z. Condensation and expansion characteristics of water steam and carbon dioxide in a Laval nozzle. Energy 2019;175:694–703.
[37] Koytsoumpa EI, Bergins C, Kakaras E. The CO2 economy: Review of CO2 capture and reuse technologies. J Supercrit Fluids 2018;132:3–16.
[38] Le Moullec Y. Conceptual study of a high efficiency coal-fired power plant with CO2 capture using a supercritical CO2 Brayton cycle. Energy 2013;49:32–46.
[39] Guo X, Chen S, Yan X, Zhang X, Yu J, Zhang Y, et al. Flow characteristics and dispersion during the leakage of high pressure CO2 from an industrial scale pipeline. Int J Greenh Gas Con 2018;73:70–8.
[40] Ding H, Zhang Yu, Sun C, Yang Y, Wen C. Numerical simulation of supersonic condensation flows using Eulerian-Lagrangian and Eulerian wall film models. Energy 2022;258:124833.
[41] Reznickova J, Petrychkovych R, Vejrazka J, Setnickova K, Uchytil P. Gas separation ability of the liquid bubble film. Sep Purif Technol 2016;166:26–33.
[42] Ounis H, Ahmadi G, McLaughlin JB. Brownian diffusion of submicrometer particles in the viscous sublayer. J Colloid Interf Sci 1991;143(1):266–77.
[43] Wang B, Xu DL, Chu KW, Yu AB. Numerical study of gas–solid flow in a cyclone separator. Appl Math Model 2006;30(11):1326–42.
[44] O'Rourke PJ. Collective Drop Effects On Vaporizing Liquid Sprays. Princeton: Princeton University; 1981.
[45] Wang X, Chang H, Corradini M, Cong T, Wang J. Prediction of falling film evaporation on the AP1000 passive containment cooling system using ANSYS FLUENT code. Ann Nucl Energy 2016;95:168–75.
[46] Liu B, Liu X, Lu C, Godbole A, Michal G, Tieu AK. A CFD decompression model for CO2 mixture and the influence of non-equilibrium phase transition. Appl Energ 2018;227:516–24.
[47] Dutta T, Sinhamahapatra KP, Bandyopadhyay SS. Numerical investigation of gas species and energy separation in the Ranque-Hilsch vortex tube using real gas model. Int J Refrig 2011;34(8):2118–28.
[48] Matheis J, Müller H, Lenz C, Pfitzner M, Hickel S. Volume translation methods for real-gas computational fluid dynamics simulations. J Supercrit Fluids 2016;107: 422–32.
[49] Lettieri C, Paxson D, Cross PB, Spakovszky Z. Characterization of Nonequilibrium Condensation of Supercritical Carbon Dioxide in a de Laval Nozzle. J Eng Gas Turbines Power 2017;140:41701.
[50] Roache PJ. Quantification of uncertainty in computational fluid dynamics. Annu Rev Fluid Mech 1997;29(1):123–60.
[51] Teixeira AM, Arinelli LDO, de Medeiros JL, Araújo ODQF. Sustainable offshore natural gas processing with thermodynamic gas-hydrate inhibitor reclamation: Supersonic separation affords carbon capture. Chem Eng Res Des 2022;181:55–73.